Hydrodynamics of mangrove-type root models: the effect of porosity, spacing ratio and flexibility

Bioinspiration & Biomimetics

PAPER

Hydrodynamics of mangrove-type root models: the effect of porosity, spacing ratio and flexibility

Amirkhosro Kazemi[1], Keith Van de Riet[2] and Oscar M Curet[1,3]

[1] Department of Ocean and Mechanical Engineering, Florida Atlantic University, Boca Raton, FL, United States of America
[2] School of Architecture and Design, University of Kansas, Lawrence, KS, United States of America
[3] Author to whom any correspondence should be addressed.

E-mail: ocuret@fau.edu

RECEIVED
9 February 2017

REVISED
19 June 2017

ACCEPTED FOR PUBLICATION
29 June 2017

PUBLISHED
20 September 2017

Keywords: mangrove root, drag force, porosity, flexibility, fluid dynamics, bio-inspired design, vortex structures

Abstract

Mangrove trees play a prominent role in coastal tropic and subtropical regions, providing habitats for many organisms and protecting shorelines against high energy flows. In particular, the species *Rhizophora mangle* (red mangrove) exhibits complex cluster roots interacting with different hydrological flow conditions. To better understand the resilience of mangrove trees, we modeled the roots as a collection of cylinders with a circular pattern subject to unidirectional flow. We investigated the effect of porosity and spacing ratio between roots by varying both the diameter of the patch, D, and inset cylinders, d. In addition, we modeled hanging roots of red mangroves as cantilevered rigid cylinders on a hinge. Force and velocity measurements were performed in a water tunnel (Reynolds numbers from 2200 to 11 000). Concurrently, we performed 2D flow visualization using a flowing soap film. We found that the frequency of the vortex shedding increases as the diameter of the small cylinders decreases while the patch diameter is constant, therefore increasing the Strouhal number, $\mathrm{St} = \frac{fD}{U}$. By comparing the change of Strouhal numbers with a single solid cylinder, we introduced a new length scale, the effective diameter. The effective diameter of the patch decreases as the porosity increases. In addition, we found that patch drag scales linearly with the patch diameter but decreases linearly as the spacing ratio increases. After a spacing ratio of ($\frac{L}{d} > 4.5$), the force scales linearly with the free stream velocity, and the mean velocity behind the patch is independent of the Reynolds number and the patch effect disappears. For flexible cylinders, we found that a decrease in stiffness increases both patch drag and the wake deficit behind the patch in a similar fashion as increasing the blockage of the patch. This information has the potential to help in the development of methods to design resilient bio-inspired coastline structures.

Nomenclatures

D	Patch diameter
d	Root diameter
a	Frontal area per unit volume
A	Projected area
C_D	Drag coefficient per unit area
St	Strouhal number
Re	Reynolds number
U_∞	Free stream velocity
Φ	Porosity
β	Solid volume fraction (solidity)
$\frac{L}{D}$	Spacing ratio
$\frac{X}{D}$	Non-dimensional distance behind the patch
λ	Vortex shedding wavelength
U^*	Velocity of vortex street
U	Time-averaged velocity
L_1	Steady wake length

Introduction

Mangrove vegetation plays a major role along shorelines and provides protection to coastal areas and estuaries from storm surges and tsunamis [1–4]. In tidal flow, mangroves can induce local flow resistance by increasing drag force, which leads to a reduction in water velocity and a decrease in shear stress that has a key role in sediment transport and erosion [5–7]. Mangrove forests, found in tide-dominated flow regions, are characterized by their massive and complex root systems (figure 1), which play a prominent role

Figure 1. Complex mangrove root systems cope with salt water immersion in tidal flows in Florida.

in the flow structure of water currents [7–9]. The main motivation of this research is to investigate the hydrodynamic effects of the mangrove root system by introducing a simplified model and exploring its influence on current flow under controlled conditions, as well as to gain an enhanced understanding of the fluid structure in the natural mangrove environment.

In this work, we performed force and flow measurements to comprehend the relationships between the drag coefficient of the root patch model of mangroves and the porosity, spacing between roots, and flexibility. We extend our experiment to flexible individual roots within the array to describe the details of the wake structure. In particular, this work is motivated by the following questions.

1 What is the implication of geometrical parameters, including porosity and spacing ratio, on the flow structure after the physical model of mangrove roots?
2 What is the effect of flexibility in the simplified case of the elastically mounted rigid roots on drag coefficient and the wake region?

For this work, we explore these questions experimentally using physical models composed of a patch of circular cylinders where we manipulate their arrangement. Additionally, we consider a simple physical model where the cylinders are hinged, allowing motion in one direction for different stiffness.

The hydrodynamics of mangrove vegetation swamps have been explored in multiple studies [10–15]. Previous studies on mangrove hydrodynamics indicate that the intricate circulation generated in water through mangrove roots dominates the flow. To date, a few studies have been conducted to understand the influence of mangrove prop roots on hydrodynamics [10, 11, 16]. Furukawa *et al* found that the mangrove roots generate complex 2D flow fields and regions with jets, eddies, root-scale turbulence, and stagnation. However, systematic research on the interaction of water flow and mangrove root systems and the implications of sediment transport has received less attention. Also, it is challenging to obtain reliable field measurements of the velocity profiles, especially when there are very short tidal periods for such measurements [17–19]. Hence, there is a need for a systematic model of the mangrove root system, and to introduce flow parameters to study its hydrodynamics. For that reason, our objective is to create physical models such that key parameters of mangrove root models can be systematically varied.

In this work, we modeled the mangrove root system with varying arrays of circular cylinders. An array of circular cylinders is often used to model rigid emergent vegetation because it provides a good approximation of the root [20, 21]. Vandenbruwaene *et al* [22] found that the initial growth of roots often forms circular cylinders. Researchers have used cylinder arrays to estimate the bulk drag coefficient [23–26]. Only a few studies have considered a finite patch of an emergent model with length and width scales smaller than the channel width [9, 20, 21, 27–30].

Previous work has studied different aspects of flow structure behind finite circular patches. Nicolle and Eames [31] and Zong and Nepf [20] described the wake behind a circular staggered patch. The numerical study by Nicolle and Eames investigated the flow behavior downstream and through the circular cylinders. They modeled a patch and changed the number of cylinders within the patch to change porosity. Chen *et al* [21] modeled seagrass vegetation as an array of circular cylinders. They ran the experiment for the flow in the region of the circular patch and studied the flow behind the patch. In comparison with a solid obstruction, they found that the flow passes through the patch, which is a porous cylinder, and delays the onset of the von Kármán vortex street due to the porosity of the patch. Chen *et al* considered changing the porosity by changing the outer diameter of the patch. Nicolle and Eames also changed porosity by changing the number of cylinders per area of patch studied. In this research, our objective is to focus on the flow behind the mangrove roots which, due to variation of diameters, spacing and rigidity, most likely will have a different flow nature compared to other underwater vegetation.

The trunk and some parts of the mangrove root are flexible, especially during the growing stage [32]. The trunk and roots oscillate in a tidal-dominated flow and act as a filter for sediments [5, 33].The flexibility of mangrove prop roots has received little attention, which resulted in difficulties in simulating the effects of prop roots in physical hydrodynamics

model experiments. Strusińska-Correia [34] modeled the trunk and the canopy using plastic branches with leaves. They tested their models in a wave tank, which was impacted by tsunami-like solitary waves of varying heights, propagating in different water depths. However, the effect of the changing flexibility parameter on the wake flow was not considered in the tidal-dominated currents.

In this work, we extend our porosity study cases to 51%. As Mazda *et al* [3] and Furukawa *et al* [32] reported, the porosity in mangroves is as low as 55%. The models were tested in a water tunnel for a range of Reynolds numbers from 2200 to 11 000. We measured drag force and compared our results with those of Chen *et al* [21], who estimated the drag force based on stem Reynolds numbers from Tanino and Nepf [25]. In addition, we related the energy in the vortex shedding period with the porosity. Also, we present the 2D flow visualization results to illustrate the relationship between porosity and Strouhal number based on the patch diameter. We visualized the small-scale turbulence region generated by the root-type cylinders. In addition, we measured the instantaneous streamwise velocity downstream of the models and compare our velocity results with those of Ortiz *et al* [28][4] and Chen *et al* [21]. They reported the highest and lowest porosities, respectively. We found the trend that the steady wake length (L_1) changes with respect to the porosity. Since, for the same porosity, L_1 decreases as D decreases [20], we compared the length scale with Follett and Nepf [29] with the same patch diameter ($D = 9$) and present its implication on the sediment deposition described by Ortiz *et al* [28][5].

We introduce an effective diameter for a patch of circular cylinders by comparing the frequency of the vortex shedding of the patches with an individual cylinder. We show the dependence of the effective diameter on porosity. Additionally, we investigated the effect of spacing ratios of a fixed number of cylinders in the patch on the patch-scale drag coefficient and velocity at mid-depth to find the patch velocity features for high and low spacing ratios. Lastly, we characterized the wake region for a flexible patch and compared it to the rigid structure counterpart. The flexibility of the root-type cylinders was modeled with an elastic connector with one degree of freedom, so the rigid cylinder that is joined to the connector can freely oscillate in the transverse direction.

Methods

In the following sections, three case studies are presented, and the geometry of physical models and the details of the experimental setup are described. Also, the design of the experiments to qualitatively and quantitatively capture the wake region, velocity profile and drag force are explained.

Physical models

We conducted a series of experiments to understand the fluid dynamics behind the mangrove root-type cylinders. Three sets of experiments were designed to investigate the influence of porosity, spacing ratio, and flexibility in the arrays of cylinders, which represent patches of mangrove roots.

Here, the diameter of each cylinder (d) in the patch is named the 'root diameter', and the outer diameter of the whole array of cylinders (D) is referred to as the 'patch diameter'. Each patch consisted of an acrylic plate and dowel rod cylinders, which were fitted through the plate with a line arrangement and were held by another thin plate to make the cylinder stand upright, extended from the bed through to the water surface. The cylinders had a modulus of elasticity equal to 10 GPa in all cases. Each case was exposed to five different inlet velocities with a certain Reynolds number. The Reynolds number was calculated based on the patch diameter and the free stream velocity. The velocities ranged from 2.3 $\mathrm{cm\,s^{-1}}$ to 11.91 $\mathrm{cm\,s^{-1}}$ and the corresponding Reynolds numbers were in a range of 2214–11 269.

We considered a 2D plane for the measurements. The origin of the coordinate is the midline at the end of the patch. The axis is in the streamwise direction with $X = 0$ at the trailing edge of the patch, and the Y axis is in lateral direction with $Y = 0$ at the centerline. For the porosity study, the cross-sections of the patches are presented in figure 2. The patch diameter is constant, and by changing the root diameter, porosity increases from left to right as shown in the figure. By changing the root diameter, the spacing ratio changes slightly compared to the porosity change.

We considered four arrays of cylinders, cases 1–4, to find the impact of porosity downstream of the patch. These cases had the same patch diameter of 9.5 cm and they have 49 cylinders in total. The configurations are shown in figure 2. The properties of each case are summarized in table 1. The porosity of the mangrove root system was computed based on the ratio of the submerged root volume to the total defined volume, to calculate the drag force induced by the presence of mangrove roots.

For the spacing ratio study we defined the spacing ratio as $\frac{L}{d}$, which is the ratio of center-to-center between two adjacent cylinders to one individual cylinder diameter (figure 3). The arrangement consisted of one cylinder in the center and eight cylinders around it. We kept the number of cylinders and the diameter of the individual cylinders constant, and changed the spacing ratio by changing the distance of the individual cylinders to expand them diagonally. Cases 9–13 correspond to different spacing ratios changing from 1.5 to 7.5, as shown in figure 3.

[4] The MIT Faculty has made this article openly available. Please share Citation Accessed Citable Link Detailed Terms Mean and turbulent velocity fields near rigid and flexible plants and the implications for deposition.
[5] See footnote 4.

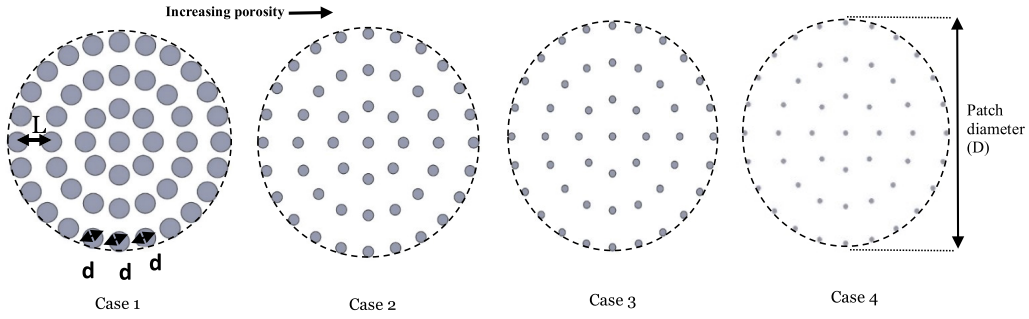

Figure 2. Physical model configurations for set 1, porosity study. Outer diameter in all cases was $D = 9.5$ cm. The porosities for cases 1–4 are 51%, 78%, 88% and 94% respectively. The porosity of the patch is described by $\varphi = 1 - \beta$, where β is patch solidity and defined by $\beta = \frac{n\pi d^2}{4}$ in which $n = \frac{a}{d}$ is the number of cylinders per unit bed area and a is frontal area per unit volume. In set 1 the spacing ratio ranges from 1.5 to 4.8 for these cases.

Table 1. Summary of cases. For each case, we ran experiments for five upstream velocities ranging from 2.3 to 11.9 cm s^{-1}.

Experiment sets	Case No	Flexural stiffness in N mm^{-1}	Frontal area (a) in m^{-1}	Patch diameter (D) in mm	aD	Root diameter (d) in mm	Porosity % (φ)	Spacing ratio ($\frac{L}{d}$)	Wake length ($\frac{L_1}{D}$)
Set 1: porosity study	1	Rigid	65.8	95	6.25	9.52	50.7	1.5	—
	2	Rigid	43.89	95	4.17	6.35	78.1	2.3	4.21
	3	Rigid	32.9	95	3.12	4.76	87.6	3.1	5.26
	4	Rigid	21.2	95	2.08	3.17	94.5	4.8	6.31
	5	Rigid	N.A	10	N.A	10	0 (one circular cylinder)		—
	6	Rigid	303	10	3.03	2.65	36	1.4	—
	7	Rigid	189	10	1.89	1.65	75	2.5	3.5
	8	Rigid	114	10	1.14	1	91	4	5.75
Set 2: spacing ratio study	9	Rigid	112.78	25.4	2.86	6.35	43.7	1.5	—
	10	Rigid	36.9	44.4	1.69	6.35	81.6	3	2.92
	11	Rigid	18.0	63.5	1.14	6.35	91	4.5	—
	12	Rigid	10.8	82.5	0.88	6.35	94.6	6	—
	13	Rigid	7.0	101.6	0.71	6.35	96.48	7.5	—
Set 3: flexibility study	14	2.15	36.9	63.5	1.69	6.35	91	4.5	1.5
	15	17.20	36.9	63.5	1.69	6.35	91	4.5	1.7
	16	58.07	36.9	63.5	1.69	6.35	91	4.5	—
Ortiz *et al*	17	Rigid	5.95	420	2.5	6.4	97	—	6.6
Zong and Nepf	18	Rigid	7	120	0.84	6	96	—	6.6
Chen *et al*	19	Rigid	86	100	8.6	6.4	57	—	—
Follett and Nepf	20	Rigid	20	100	2	6.4	90	—	4.2

For the flexibility study, we used flexible connectors and attached the solid cylinders to the bottom so that the flexible connectors were capable of oscillation only perpendicular to the flow. By changing the thickness of the material, we fabricated connectors at three flexural stiffness: 2.15, 17.20 and 58.07 N mm^{-1} (see figure 4). For cases 14–16, the diameter of the patch was $D = 6.35$ cm, and the diameter of each cylinder was $d = 6.35$ cm. The tops of the connectors were fixed to a plate, and the cylinders were hanging, which enables the flexible connectors to oscillate from side to side perpendicular to the direction of the flow.

The flexible connector was made from ABS Plus, Stratasys 3D printing material, with a flexural modulus (E) of 300 000 psi. To calculate the flexural stiffness, we applied Hooke's law and replaced deflection with lateral force. Therefore, the flexural stiffness was calculated based on the following equation:

$$K = \frac{E \cdot W \cdot t^3}{4L^3} \quad (1)$$

where E is the modulus of elasticity, w is the width, t is thickness and L is the length of a cantilever beam.

Experimental setup and instrumentation

All experiments to measure force and flow were performed in a low turbulence re-circulating flume with a test section 2 meters long and with a cross-sectional area of 250 mm × 250 mm. We submerged

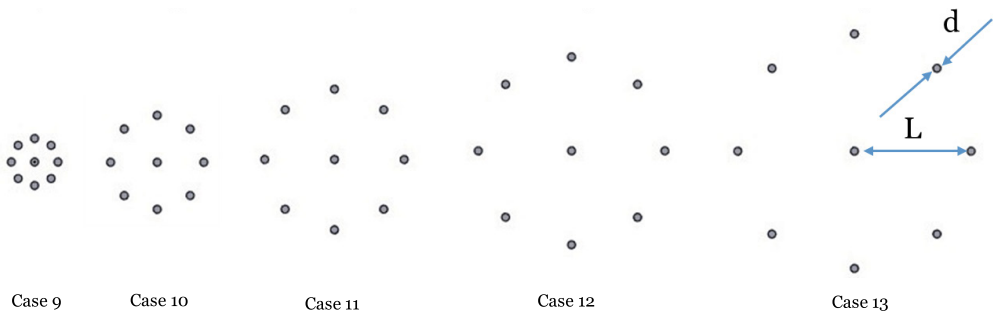

Figure 3. Physical model configurations for set 2, spacing ratio study. There are five cases with the same number of cylinders per patch, with the same root diameter ($d = 0.63$) but a different center-to-center distance in each case. Cases 5–9 correspond to spacing ratios of 1.5, 3, 4.5, 6 and 7.5, respectively.

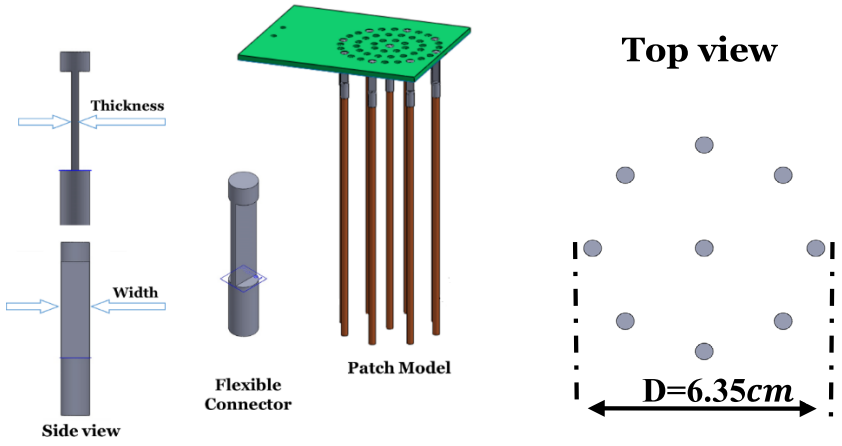

Figure 4. Schematic of the flexible connector and the patch setup. The connectors are shown in different views: left is the side view, right is the top view and the middle shows connectors attached to a plate and cylinders. For all cases, the diameter of the patch is $D = 6.35$ cm, the diameter of each cylinder is $d = 0.63$ cm, and the porosity and spacing ratio are 91% and 4.5 respectively. The tops of the connectors were fixed to a plate, and the cylinders were hanging, which enables the flexible connectors to oscillate from side to side. The flexibility is defined based on the flexural stiffness of a cantilever beam and changes from 2.15 to 58.07 N mm^{-1}.

the mangrove root-type models in the middle of the flume, 70 cm from the inlet of the test section and attached to an air-bearing system capable of moving frictionlessly in two directions, along and perpendicular to the water tunnel (figure 5). A 9-N load cell (Futek LSB200) was attached to the air-bearing system to measure the total drag force of the patch along the flume, and therefore restricting the motion of the model along the flume axis. An acoustic Doppler velocimeter (ADV-Nortek Vectrino) was set up in the tunnel to measure the velocity behind the patch in the midline, and it was manually traversed along the flume behind the patch at 12 locations with an accuracy of ± 1 cm. The sampling frequency of the flow measurement was 200 Hz. Based on previous studies with emergent obstructions [35], the velocity measured at mid-depth is a good approximation of the depth-averaged velocity, which may be used to represent the approximately 2D behavior of the flow [20]. The sampling volume for velocity measurement was 6 mm across and 3 mm high. In this work, we measured three components of velocity, but we present only the streamwise and transverse components. We used a vertical component to check if the orientation of the probe was consistent in different locations and manual traversing was horizontal for each test case. We repeated the experiment at five velocities ranging from 2.3 cm s^{-1} to 11.9 cm s^{-1}, which varied based on the pump frequency of the flume. Data acquisition at each measurement point was 60 s with a sampling frequency of 1000 Hz for force data. We recorded the time-average and the fluctuation components at each measurement point.

In the next step, we analyzed the data by plotting variations of force with respect to time and mean velocity. We obtained an average drag force measurement at each velocity. Calibration was conducted by measuring the voltage output of the load cells for five weights. The output of the load cell was an analog signal, converted to digital by NI 9052 A/D Card. For data acquisition, Matlab codes were used to find the best linear fit to convert volts to force.

Flow visualization

We visualized the wake behind the array of roots using a vertical soap film setup. The soap film is a convenient experimental system that resembles a 2D flow pattern [36, 37]. In this study, the flow visualization

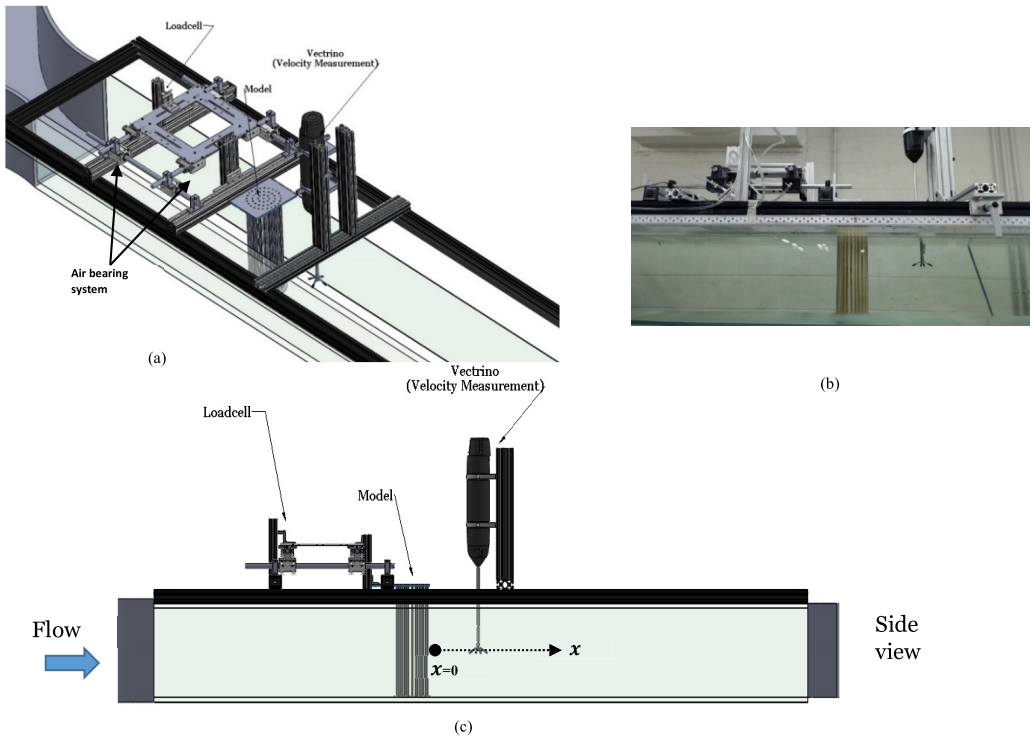

Figure 5. (a) Experimental setup for drag and velocity measurement in the water tunnel. Models were placed in the middle of the flume, attached to a frictionless air bearing system capable of moving with two degrees of freedom. (b) Mounted model on water tunnel at FAU-Seatech. The depth of the water was 25.4 cm. (c) Side view of the water tunnel showing the direction of the inlet flow; the length of each cylinder was 40.64 cm, but only 22 cm was submerged. All cases were exposed to five inlet velocities ranging from 2 cm s^{-1} to 10 cm s^{-1}.

experiment was performed with a gravity-driven soap film apparatus located at Florida Atlantic University. A schematic of the soap film setup is displayed in figure 6, which indicates the soap film configuration. The soap film consists of water and Dawn dishwasher detergent, with a 4% soap concentration. The soap flows from top to bottom with a constant velocity. The soap flows through two thin nylon wires of 0.4 mm diameter, which separate at a nozzle with an 0.8 mm inner diameter. The horizontal span of the tunnel was 10 cm, and the typical film thickness was 3–4 μm. The spreading angle of the wires at the top was around 10°. The wires attached to the bottom of the reservoir kept the soapy water at a constant pressure head by means of a pump that regulates the flow rate.

We tested four patches (cases 5–9) in the soap film. The patches were made of stainless steel cylinders fitted in a plexiglass plate. All patches had an outer diameter of $D = 10$ mm, but different individual cylinder diameters produced porosities ranging from 36% to 91%. The geometrical properties of the tested patches are presented in table 1 for cases 5–9. We inserted the patch half the length of the cylinders into the soap film. The flow was visualized using a low-pressure sodium lamp as the monochromatic light with a wavelength of 600 nm illuminating the soap film. Then we captured the wake using a high-speed camera, a Fastcam UX 50, with 1000 frames per second. The resolution of the camera was 1280 × 1024 pixels and the recording time was 20 s. The Reynolds number for the patch is given by $\mathrm{Re} = \frac{UD}{\upsilon}$ where U is the upstream flow speed, D is the patch diameter and υ is the kinematic viscosity of the soap film. We used the kinematic viscosity

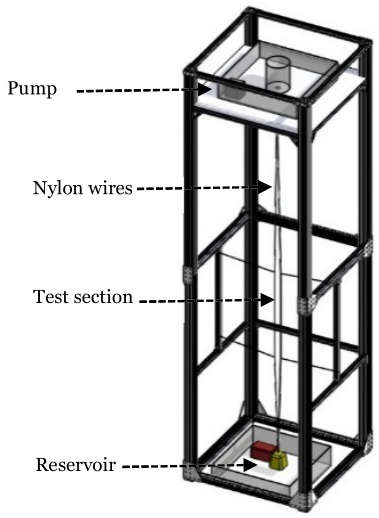

Figure 6. Experimental setup for mounting the patch soap film apparatus. The size of the test section is 20 cm long and 8 cm wide. We used two thin nylon wires with soap film hanging between. The bottom reservoir contains a soapy solution made with water and 4% of dishwasher detergent. We used a pump to recirculate water from reservoir to injection nozzle, where the thin film is formed until it reaches the reservoir. The experiments were performed in the midline of the channel, 60 cm below the flow inlet. Arrays of cylinders with the same patch diameter but porosities varying from 36% to 91% were inserted into the film.

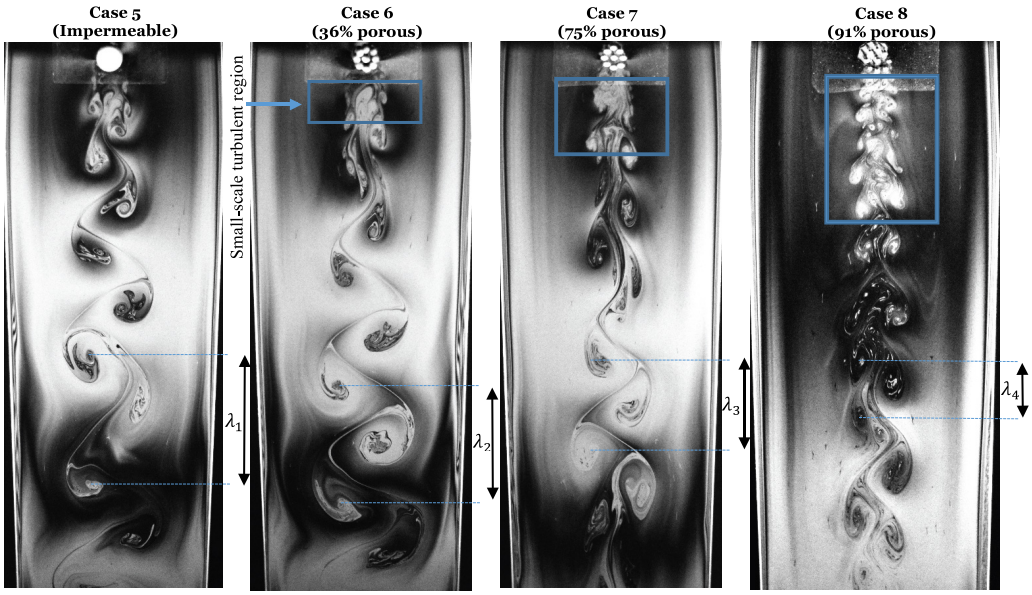

Figure 7. Soap film experiment flow visualization snapshot of von Kármán vortex street behind arrays of nine cylinders for impermeable and porous patches. The delayed onset of the von Kármán vortex street is pictured for Re = 1400 in cases 5–8. We observed two regions behind the patch associated with small-scale turbulence (as shown in frames) of individual cylinders and formation of a 2*S* mode wake. λ is the wavelength of the vortex street, which is reduced by increasing the porosity.

reported by Wu [38]; that is, in the order of 10^{-6} m^2 s^{-1}. The velocity of incoming flow was 2 m s^{-1}, which was approximated by motion tracker at the center of the channel, and the corresponding Reynolds number was 2×10^4.

Results and discussion

The experimental results from the soap film and the water tunnel experiments are shown in the following sections. The quantitative results in the water tunnel, including drag forces and mean velocity behind the patch, are presented in three sections for the porosity, spacing ratio, and flexibility experiments.

Soap film experiment

The snapshot of the roots and results from the soap film experiment are presented in figure 7. The wake formation for different porosities is shown and compared with a rigid non-porous root wake.

Figure 7 shows the instantaneous flow pattern revealing a sequence of vortex shedding behind the different cases forming a von Kármán vortex street. For the solid root, the soap film is formed into the von Kármán vortex street immediately downstream of the obstruction. For porous patches, we detected two main wake regions that are studied in this research:

(a) the interaction of multiple eddies immediately behind the patch forming the small-scale vortex structure, and;

(b) development of an asymmetric wake further downstream of the patch forming a von Kármán vortex street.

We observed the generation of a small-scale turbulent wake region directly behind the porous patches. In this region the vortices are turbulent, and eddies begin to interact directly after passing the patch downstream of the roots. The vortices act together in such a way that the rows of eddies approach one another until all eddies lie in a single row on the wake axis. The small turbulent vortices recombine in larger vortex structures forming the von Kármán vortex street. The region of small-scale turbulence increases with porosity. Also, it can be observed that the distance between von Kármán vortex street, λ, decreases as the porosity of the patch increases.

The main vortex pattern near the region is the 2*S* mode, which means one vortex is generated in each half of the shedding cycle. The vortex street formed behind patches remains stable further downstream of the patch. By increasing porosity, the beginning of the vortex street is located further downstream of the patches, and the vortex street narrows, indicating a decrease in the strength of the vortices. By changing the porosity, the vortex pattern remains as 2*S* mode, similar to the single impermeable cylinder.

Furthermore, we analyzed the images to approximate the variation of Strouhal numbers for different porosities. Strouhal number is determined by:

$$\mathrm{St} = \frac{fD}{U} \tag{2}$$

where f is the frequency of the vortex shedding, D is the patch diameter and U is the upstream velocity. The vortex shedding period, T, is the inverse of f and is defined by:

$$T = \frac{\lambda}{U^*} \tag{3}$$

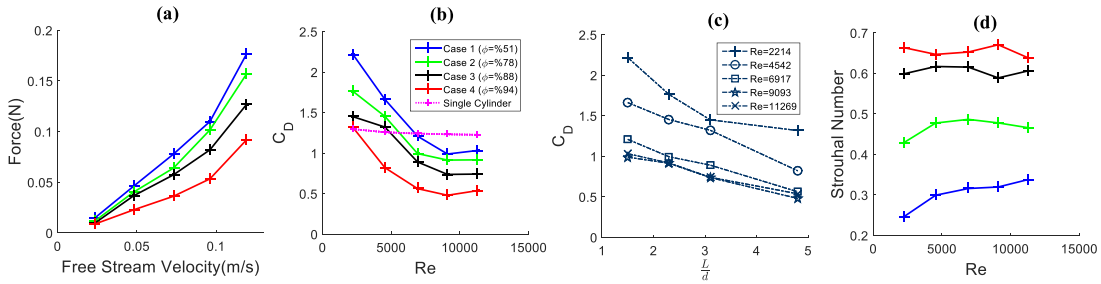

Figure 8. Drag force coefficient in stream-wise direction for different porosities for cases 1–4: (a) drag force on the entire patch changes for different inlet velocities, (b) drag coefficient with respect to Reynolds number by considering the outer diameter as characteristic length scale; (c) drag coefficient with respect to the spacing ratio for porosity experiments, and; (d) Strouhal number as a function of Reynolds number for various patch porosities.

where λ is the wavelength of the vortex street and refers to the distance between the generation of two consecutive vortices, and U^* is the velocity of the von Kármán vortex. By approximating that the vortex is moving at the speed of the upstream velocity, one can rewrite the Strouhal number by:

$$\mathrm{St} = \frac{D}{\lambda}. \tag{4}$$

Therefore, the Strouhal number has an inverse relationship with the wavelength of the vortex street. Based on equation (4) we calculated the Strouhal number for case 5 (high porosity) to case 8 (a solid cylinder) as equal to 0.5, 0.3, 0.23, and 0.21, respectively. Thus, by increasing porosity the Strouhal number also increases as the distance between two shed vortices decreases.

Porosity experiment

By increasing the free stream velocity, the net force on the entire patch increases quadratically (figure 8(a)). The trend of the increasing force is similar to one circular cylinder and shows that, by increasing the velocity, the resistant force will be increased. Figure 8(b) shows that the drag coefficient depends on both the Reynolds number and porosity. By increasing the Reynolds number, the drag coefficient of the entire patch decreases for all porosities. To calculate drag coefficient, we used the patch diameter as the characteristic length, as follows:

$$C_\mathrm{D} = \frac{F}{1/2\rho A U^2} \tag{5}$$

where A is the projected area of the patch based on the patch diameter and the length of submerged portion of the patch, F is the drag force, and U is the freestream velocity.

It is interesting to note that the drag coefficient for one circular cylinder, for Re = 2214 to 11 269, is marginally changing with Re, but in our experiments the drag coefficient for the patch is dependent on Re. In addition, the drag coefficient decreases with an increase of porosity. As more roots are packed together, the drag coefficient tends to the value of a solid cylinder, which is approximately $C_\mathrm{D} = 1.22$ for the plateau region. For a smooth circular cylinder, C_D decreases for small Re numbers until it reaches a minimum at around Re $\approx$ 1000, then increases slightly and reaches a plateau from Re $\approx 10^4$ to 10^5 before it drops due to turbulence [39].

The change in drag coefficient is most likely due to the hydrodynamic interaction inside the patch. As porosity decreases, the spacing between the roots will be less, and the upstream velocity for individual roots is the wake velocity for the upstream root within the patch. Consequently, the velocity drops in the patch continuously. Therefore, the bleed flow through the patch close to the trailing edge will decrease tremendously and the behavior of the patch will be similar to that of a solid cylinder. In contrast, by increasing porosity, the spacing between the roots will grow, and the vortex street of the individual roots within the patch is annihilated by wake interactions. Thus, the arrangement of the cylinders within the patch behaves as uncoupled cylinders, and the individual cylinder wake is generated. The uncoupled individual cylinder wake at high porosity was observed by Nicolle and Eames [31], Takemura and Tanaka [19] and Chen *et al* [21]. As a result, the flow can pass through the individual roots at a higher velocity and the bleed flow from the patch increases, which delays the interaction of the shear layers and formation of the von Kármán vortex street.

Figure 8(c) shows how the drag coefficient drops by increasing the spacing ratio. Since the patch diameter (D) is the same for all patches, the Reynolds number does not change with a constant upstream velocity. There is a higher change in drag coefficient at lower Reynolds numbers, and the drag coefficient varies considerably with respect to the spacing ratio. However, at higher Reynolds numbers (Re $\geqslant$ 8917), the change is less, indicating that the impact of the spacing ratio is insignificant at higher Reynolds numbers. Moreover, the effect of the Reynolds number at higher velocities is much less than at lower velocities.

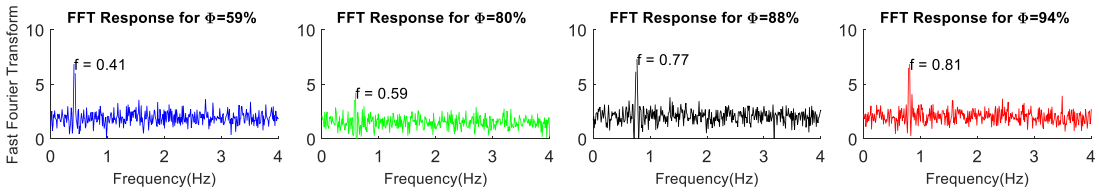

Figure 9. FFT plots of the flow forces for different porosities at Re = 11 269. The frequency of the first peak of the plots is selected as the frequency of vortex shedding.

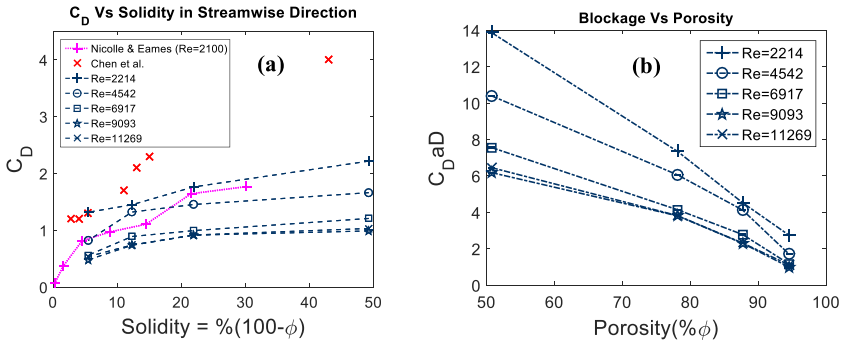

Figure 10. (a) Variation of drag coefficient with solidity ($\beta = 1 - \varphi$) for different Reynolds numbers. The results are also compared with the numerical study by Nicolle and Eames [31] and the experimental study by Chen *et al* [21]. (b) Blockage parameter ($C_D aD$) changes with respect to porosity.

The frequency of vortex shedding was found by spectral analysis performed on the force signal. We assumed that the peak in the force signal spectral analysis indicates the dominant frequency of the vortex shedding. Figure 9 shows the fast Fourier transform (FFT) of the forces signal for different porosities at Re = 11 269.

The Strouhal number seems to be changing slightly with the Reynolds number over the range of Re, and we found no evidence of the chaotic behavior of the velocity fluctuations in the wake (figure 8(d)). The figure confirms that the Strouhal number is almost constant for various Reynolds numbers, but is increasing with porosity. This is consistent with our flow visualization results. One can infer that, as the porosity of the patch increases, the wavelength of the vortex street decreases, the distance between two vortices decreases, and the Strouhal number increases.

Figure 10(a) indicates that the drag coefficient grows with solidity. The results for different Reynolds numbers are compared by Nicolle and Eames [31] and Chen *et al* [21]. Nicolle and Eames reported their numerical study results for a Reynolds number of 2100. The experimental results of Chen *et al* are for a range of different Reynolds numbers. The trends are similar for all Reynolds numbers; with an increase in solidity, there is a higher drag coefficient.

Chen *et al* estimated the drag force from Tanino and Nepf [7] based on solidity, the stem (d) Reynolds number, was based on the average velocity within the patch. The drag coefficient, C_D, can be affected by the stem density, the stem Reynolds number, and the morphology of the individual canopy elements [7, 15]. Unfortunately we could not measure the average velocity within the patch due to engineering constraints. However, since the cylinders in our patch have in-line arrangements, the local velocity in the patch could achieve higher values compared to a staggered patch. In the staggered patch, which was used by Chen *et al*, the flow obstruction is higher, hence the mean value within the patch has lower values and thus lower Reynolds numbers. Therefore, based on Tanino and Nepf [7], the drag coefficient will be higher than in our case. We found agreement with the numerical solutions of Nicolle and Eames and Chen *et al*, over the range of $3 <$ solidities < 15. At lower solidities, the cylinders are far apart in the patch so that the configuration has less effect on local velocity within the patch. Consequently, the resistance to the water flow, implying drag coefficient, is in reasonable agreement with our results.

The flow structure can be characterized by a non-dimensional flow blockage parameter, $C_D aD$, which is the ratio of the patch diameter to drag length scale $(C_D a)^{-1}$. Flow blockage indicates the blockage of the patch when flow passes through it and describes the flow adjustment to a long, circular patch of finite diameter D [21]. We found a decreasing blockage with increasing Reynolds number only in low porosity cases. In the higher porosity cases, there is little change in the blockage with varying Reynolds numbers (figure 10(b)). The trend indicates the combined impacts of the frontal area and drag coefficient by changing the porosity. Notice that the trends for blockage parameters are similar for all Reynolds numbers, and that

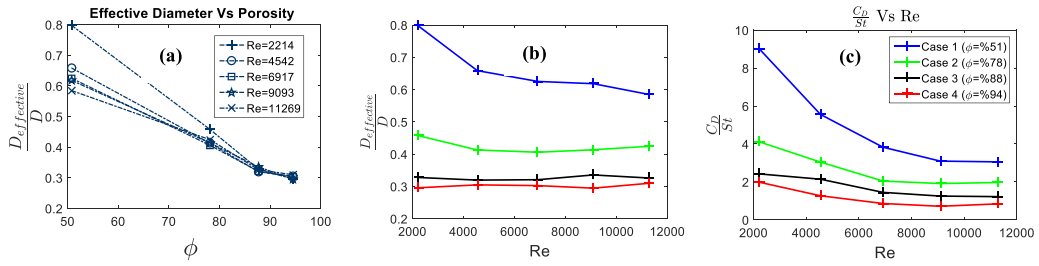

Figure 11. (a) Effective diameter normalized by patch diameter converges to approximately one-third of the patch diameter; (b) effective diameter versus Reynolds number, and; (c) energy released per vortex shedding period with respect to porosity.

they decrease by increasing the porosity. Frontal area and drag coefficient both decrease by increasing porosity. Therefore, the multiplication effect of both parameters shows that the blockage decreases drastically with respect to porosity. In addition, for porosity of more than 88%, all flow blockage parameters of patches fall below 4 so there is no recirculation zone for $C_D aD < 4$, which is in agreement with Chen *et al* [21].

By comparing the Strouhal number of the patches with a solid cylinder, one can find an effective diameter based on the wake signature. The 'effective diameter' is the diameter of an individual cylinder within the patch (a root diameter) that gives the same frequency of vortex shedding as an equivalent patch-sized cylinder. We define the effective diameter by:

$$D_{\text{eff}} = \frac{\text{St}_{\text{eff}} \times U}{f} \tag{6}$$

where St_{eff} is the Strouhal number of a solid cylinder, which equals approximately 0.2.

We observed that for all Reynolds numbers considered, as the porosity increases (or the blockage decreases), the non-dimensional effective diameter also decreases (figure 11(a)). This means that we can represent the characteristic of the unsteady flow behind the porous patch with a solid cylinder that has a smaller diameter (the effective diameter). At higher porosities ($\varphi \geqslant 88\%$), the effective diameter converges to the same particular value, approximately one-third of the patch diameter, independent of the Reynolds number. On the other hand, as the porosity decreases (blockage increases), the effective diameter increases. At lower porosities, ($\varphi \leqslant 78\%$), the effective diameter changes with Reynolds number, with an increase of effective diameter for lower Re.

We find that the effective diameter depends more on the porosity and slightly varies with the Reynolds number (figure 11(b)). As porosity increases, the effective diameter decreases. Here, one can distinguish the difference between porosity and effective diameter, where the former indicates the ratio of empty area to solid area in a volume, whereas the latter specifies the equivalent diameter of which we have the same flow pattern. Porosity is a geometrical parameter whereas the effective diameter is related to the fluid parameter. Based on figure 11(a), the change in effective diameter is much smaller at higher porosities, and as a result, the effective diameter is less dependent on higher value porosities.

The drag coefficient is an indication of how much energy is invested into the fluid per unit of time and $\frac{C_D}{\text{St}}$ is the energy released per vortex shedding period. Therefore, the Strouhal number is the conversion factor for both timescales [40]. At a given Reynolds number in figure 11(c), the least porous patch has the most energy released, which decreases rapidly as Re increases. Then, it plateaus to an approximately constant value. The reason is that for a constant Re value, a decrease in porosity causes an increase in C_D and a decrease in Strouhal number. Thus, $\frac{C_D}{\text{St}}$ will increase, which means the energy released in the period of vortex shedding is increased. Therefore, with a less porous patch, which corresponds to a higher drag coefficient, the patch will release more energy in the vortex street. Moreover, the trend of $\frac{C_D}{\text{St}}$ indicates that, for lower Reynolds numbers, the energy released per vortex changes with respect to the porosity. However, for higher Re, the difference in energy release per vortex between low porosity and high porosity decreases.

Figure 12 presents time-averaged velocities along the centerline, downstream of the patch, for different porosities and different Reynolds numbers. Figure 12(a) depicts the time-averaged non-dimensional velocity at all locations for four porosities and five Reynolds numbers. In this figure, the vertical axis represents a non-dimensional number for the velocity, which represents the ratio of time-averaged velocity to free-stream velocity. The flow patterns for a specific porosity are similar, regardless of the Reynolds numbers. This enables us to present our velocity results in Reynolds-averaged velocity in midline, as shown in figure 12(b).

The velocity profiles for the porosity study have almost U-shape trends in figure 12(b); the velocity decreases continuously until it reaches a minimum and creates a wake region. After this region, the velocity along the centerline increases to reach the upstream velocity. The U-shape velocity, behind the patch, has been previously observed by Zong and Nepf [20], Chen *et al* [21], Ortiz *et al* [28][6] and Follett and Nepf [29].

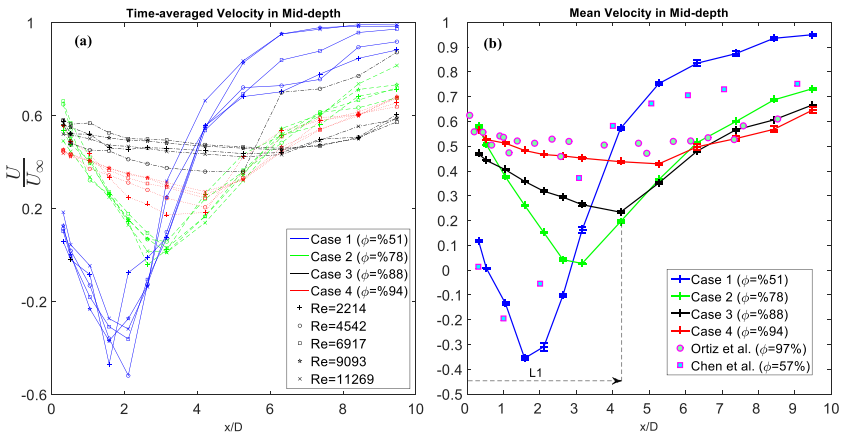

Figure 12. (a) Time-average velocity in a streamwise direction at different locations behind the patches for various porosities and Reynolds numbers. (b) Reynolds-averaged velocity behind the patch of cylinders at various locations and porosities in the midline.

It is important to note that the minimum velocity increases with higher porosity. Similarly, the location of the minimum velocity from the patch is farther downstream as the porosity increases. Accordingly, there is a compromise between the intensity of the wake deficit and the length scale of the wake L_1 depending on the porosity. (The wake length, L_1, is defined as the length between the patch and where the flow speed increases after the minimum velocity (see figure 12b).) The main cause of expansion of wake length scale is the growth of a bleed velocity from the patch. With more porosity, the bleed flow increases, which most likely postpones the interaction of the shear layers at a farther distance. Then, the shear layers interact weakly at farther distances, which induces an escalation to the minimum velocity of the wake.

At low porosities, for example when $\varphi = 51\%$, the velocity profile behind the patch is very similar to a solid body wake, and the steady wake region is absent. This is nearly identical to Chen *et al* [21] with almost the same patch diameter, showing a shift in position of the recirculation zone due to the difference in porosity ($\Delta\varphi = 6\%$). At high porosities, for example when $\varphi = 94\%$, the patch produces the patch-scale von Kármán vortex street at a farther distance from the patch. It is comparable to Ortiz *et al* [28][7] for $\varphi = 97\%$ in which the von Kármán vortex formation occurs at farther distances.

The difference between our velocity results and those of other groups (figure 12(b)) is probably due to the wall effect. The wall effect has an impact on the evolution of the wake by changing the outer velocity. As the ratio of $\frac{D}{W}$ increases, water can pass through a more constricted area. Thus, the outer velocity increases since the flow is incompressible, and momentum is assumed to be conserved. As the outer velocity increases, the length scale L_1 also increases [20]. The ratios of $\frac{D}{W}$ for Ortiz *et al* [28][8] and Chen *et al* [21] are 0.37 and 0.08, respectively. The wall effect in our experiment is 0.38; therefore, the higher wall effect creates a wider velocity profile compared to Chen *et al*; we expect to have a higher outer velocity and a larger steady wake length.

Sediment deposition in mangrove swamps depends on the particle size, the velocity, and low turbulence [28][9]. There is a minimum velocity and turbulence below which the sediments are deposited. Hence, the regions of deposition are commonly associated with regions of minimum velocity and turbulence. The minimum velocity depends directly on particle size. By using the minimum velocity, we can identify the length of enhanced deposition. The minimum velocities for coarse and fine material are $\frac{U}{U_\infty} < 0.7$ and 0.5, respectively. We considered the criteria for fine material to verify the impact of minimum velocity on enhanced deposition in mangrove swamps. Based on figure 12 (b), there is no sediment deposit region beyond approximately $\frac{X}{D} = 6.5$. Moreover, at the porosity of 88%, the magnitude of the velocity approaches zero. In this location, at $\frac{X}{D} = 3.2$, the flow stagnates locally. The location of the zero velocity is important in controlling the flow so that, at certain stagnation points, sediments can be deposited in the flow. Based on figure 12(b), we recognize that for porosities more than 78% the minimum velocity reaches zero and stagnates locally before accelerating to free stream velocity, which implies that for $\varphi > 78\%$, there is no stagnation zone occurring at any locations after the patch. The hydrodynamics as well as the sedimentation pattern in this study are relevant to unidirectional flows; however, sedimentation can be different within bi-directional flows or high wave energy [28][10].

Spacing ratio experiment

The results for different spacing ratios are presented in figures 13 and 14 for drag force and velocity

[6] See footnote 4.
[7] See footnote 4.
[8] See footnote 4.
[9] See footnote 4.
[10] See footnote 4.

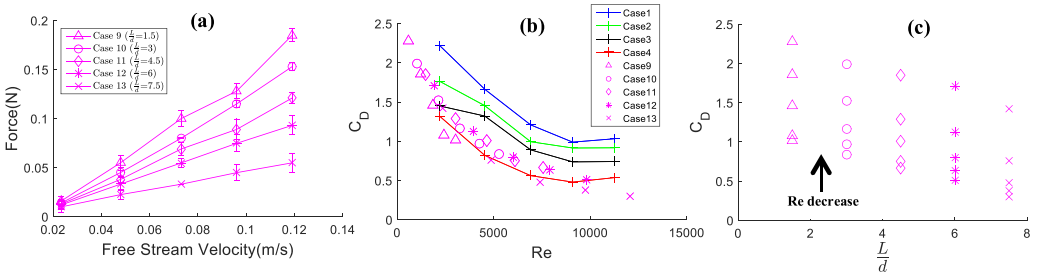

Figure 13. Force measurement results for cases 9–13: (a) drag force changing with respect to free stream velocity; (b) drag coefficient in stream-wise direction for different spacing ratios, and; (c) drag coefficient with respect to the spacing ratio for spacing ratio experiments.

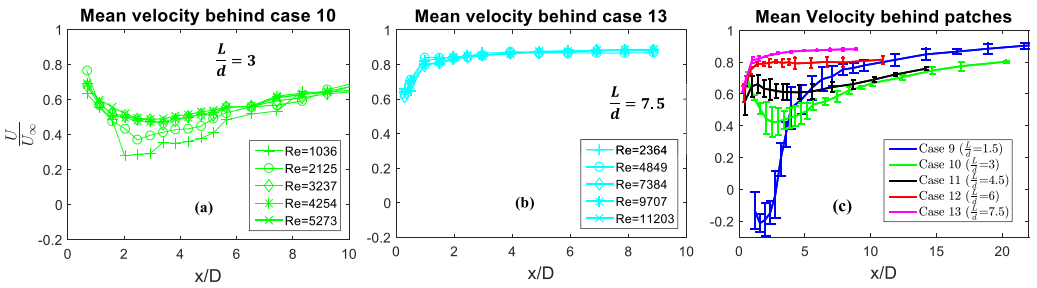

Figure 14. Non-dimensional velocity in stream-wise direction for different Re. (a) Spacing ratio $\frac{L}{d} = 3$, case 10, and (b) spacing ratio $\frac{L}{d} = 4.5$ case 13. (c) Reynolds-average velocity for different spacing ratios correspond to cases 9–13.

measurements, respectively. Smaller values of $\frac{L}{d}$ represent less distance between the roots in a patch so that the patch is more packed. By contrast, larger values of $\frac{L}{d}$ indicate greater spacing between the roots, representing sparse patches. For all spacing ratios, as the free stream velocity grows, the force on the patch increases and the drag coefficient decreases.

Our data shows that by increasing the spacing ratio, the drag force and coefficient decrease. However, the drag force has two different behaviors. For small spacing ratios, force changes quadratically with respect to the free-stream velocity. Nevertheless, after the spacing ratio $\frac{L}{d} = 4.5$, the force scales linearly with the free-stream velocity. The Reynolds number, based on the individual diameter of the roots, ranges from 147 to 754. In this range, drag force changes linearly with respect to the velocity. Thus, it seems that for smaller values of $\frac{L}{d}$ and a denser patch, the characteristic length is the patch diameter, 'D', but for higher values of $\frac{L}{d}$, the patch has features of small Reynolds numbers with the characteristic length of 'd'.

By increasing $\frac{L}{d}$, the porosity of the patch will be increased and cause lower drag force values, and concurrently, increasing $\frac{L}{d}$ grows the frontal area. Thus, the drag coefficient decreases rapidly by increasing the spacing ratio (figure 13(b)). The drag coefficient in the porosity experiment has a small shift due to the different individual diameter; however, for the spacing ratio, the drag coefficient collapses on the same curve

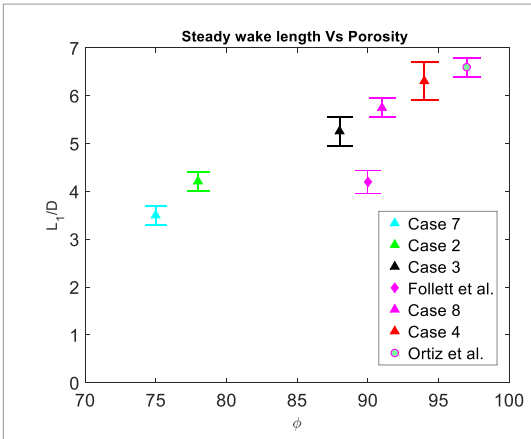

Figure 15. Steady wake length comparison for different cases with Follett and Nepf and Ortiz *et al.*

which is an indication of patch diameter drag scale. It confirms that patch diameter is an appropriated length scale of the force on the patch, as all of cases 9–13 follow a similar curve on the C_D versus Re. However, in the porosity experiment, as the root diameter changes (cases 1–4) the patch diameter is not sufficient to 'collapse' the drag coefficient data to a single curve.

Figure 13(c) shows that the drag coefficient decreases with spacing ratio. Since either the patch diameter (D) or upstream velocity changes for each case, the Reynolds number is not constant. However, at a fixed spacing ratio, drag coefficient decreases by Reynolds number. By comparing this figure with figure 8(c), one can notice the similar effect of porosity and spacing ratio on the drag coefficient; the drag

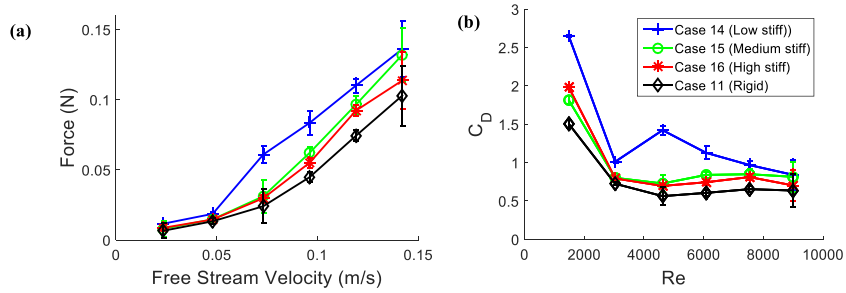

Figure 16. (a) Drag forces with respect to free stream velocities. (b) Drag coefficients in stream-wise direction for different flexibilities.

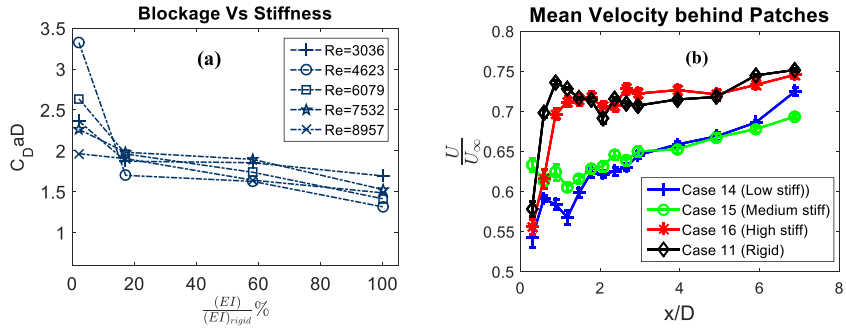

Figure 17. (a) Blockage parameter in stream-wise direction for different stiffnesses. Here stiffness is depicted as the stiffness ratio of each case over the rigid case. (b) Mean velocity profile behind the patches in stream-wise direction for three different stiffnesses and the rigid counterpart. For less flexible patches, the velocity gets to free stream velocity nearer to patch, and the wake deficit region is smaller. Nevertheless, by increasing the flexibility, the velocity magnitude behind the patch decreases considerably, and the velocity deficit region behind the patch grows.

coefficient decreases with an increase in porosity or spacing ratio and Reynolds number.

As shown in figure 14(a), the mean velocity for a lower spacing ratio ($\frac{L}{d} = 3$) changes with Reynolds number. However, by increasing the spacing ratio ($\frac{L}{d} = 4.5$), the velocity is independent of the Reynolds number (figure 14(b)). By comparing the figures, it is evident that at the lower spacing ratios, ($\frac{L}{d} < 4.5$), the velocity profile has a U-shape. In other words, immediately behind the patch, the velocity starts to decelerate until it reaches its minimum value and then accelerates to the upstream velocity. Figure 14(c) shows the change of Reynolds-averaged velocity behind the patch with respect to the patch location and different spacing ratios. For $\frac{L}{d} = 1.5$, the velocity starts from negative values, which is mainly due to the fact that the roots in the patch are very close together so that they form a coherent array of cylinders. As a result, the flow generates a stronger wake in the region close to the patch. The negative wake velocity region will enhance deposition of sediments. However, by increasing the spacing ratio ($\frac{L}{d} = 7.5$), the patch effect disappears and the velocity profile resembles the behavior of flow around a single rigid cylinder, which is in agreement with the force results. The reason is mainly because of the fact that as the patch expands diagonally, the vortex generation will be at the scale of small roots. This will decrease the interaction of the shear layers, which lessens the strength of mixing turbulence in the midline. Therefore, along the midline, there is only the wake structure similar to an isolated cylinder counterpart of one individual root, and signifying that the fluid dynamics behavior of the patch with large spacing ratio is similar to an isolated cylinder in the midline.

Figure 15 compares the steady wake length normalized by patch diameter, $\frac{L_1}{D}$, for different cases from our data, Ortiz *et al* and Follett *et al*. The steady wake length increases almost linearly with respect to the porosity. Follett and Nepf [3] reported a lower length scale compared to our results. This difference is probably due to the lower wall effect $\frac{D}{W} = \frac{10}{120} = 0.083$ compared to our results ($\frac{D}{W} = 0.38$), as discussed in the previous section.

Flexibility experiment

During the test for flexible patches, we observed lateral oscillations for all Reynolds numbers. We noted that the movement of each single root was different from each of the others. The roots close to the leading edge and trailing edge of the patch moved faster than the rest of the roots in the patch.

The results of force measurements of flexible roots are presented in figures 16(a) and (b). The velocity changes from 0 to 0.15 m s^{-1} and the force changes from 0 to approximately 0.16 N, respectively. By increasing the upstream velocity, we have more drag force and less drag coefficient. It can be noted that as the stiffness decreases

(more flexible) the drag coefficient increases. One reason is that the root oscillations can increase the turbulence region behind the patch and cause the drag coefficient to increase. The other reason is that by increasing the free stream velocity, the amplitude of oscillations will be larger, so it can enhance the frontal area that blocks the flow. As is shown in figure 17(a), the blockage parameter is depicted versus stiffness, indicating that for highly flexible patches the blockage parameter increases drastically. However, it changes slightly for less flexible ones.

Figure 17(b) shows the effect of different stiffnesses on the mean velocity behind the patch. We compared the stiffness variation with a rigid case counterpart. By comparing the trends for porosity and flexibility study, one can notice the effect of flexibility downstream of patches of roots. Unlike for the porosity study, in which there is a decreasing region followed by a growing region for velocities, they start from a minimum velocity and escalate to reach the free stream velocity for highly flexible roots so that the patch effect will disappear. It is also noteworthy that for more flexible patches, the velocity deficit is higher and it takes greater distances to recover to free stream velocity in the downstream. For that reason, the length scale of the velocity deficit region behind the patch increases compared to the corresponding rigid cases.

The results imply that the flow resistance in mangrove swamps can be properly parameterized by an increased drag coefficient, and the drag coefficient is found to vary between 0.6 and 3. Particularly at low values of velocity ($\mathrm{Re} < 2000$), C_D reaches larger values. It means that in shallow water in which there is lower velocity in mangrove swamps, dense prop roots and pneumatophores have a significant role in forming the flow field in mangrove areas. For $\mathrm{Re} > 6000$, the drag coefficient tends to converge towards constant values. As the drag coefficient depends on the flexibility of the roots, it suggests that the flow resistance in mangrove vegetation in shallow water will depend greatly on the flexibility. However, in a region of water with higher velocity, the flow resistance changes only slightly with the flexibility of the mangrove prop roots.

Conclusion

We studied the complex interaction of water flow and mangrove roots, which were modeled with a circular array of cylinders with different porosities, spacing ratios, and flexibilities. Using soap-film flow visualization we compared the wakes of porous patches with an impermeable cylinder qualitatively. The results revealed a small-scale turbulent wake region behind porous patches. The turbulent region is generated due to the interaction of multiple eddies immediately behind the patch, which reorganize after a certain distance and form a von Kármán vortex street. Also, as porosity increases the distance between two vortices reduces, indicating an increase in Strouhal number with porosity.

We introduced an effective diameter for a patch of circular cylinders by comparing the frequency of the vortex shedding of the patches with an individual cylinder. We found that D_{eff} is dependent on the porosity and slightly changes with Re. The effective diameter based on the frequency of vortex shedding is less than the patch diameter. This trend of changing effective diameter indicates that for higher porosities, the effective diameter difference between higher and lower porosity decreases. Our finding shows that C_D for the porous patches is dependent on the Re range of 2214–11 269 using the diameter of the patch as the length scale. The C_D behavior of the patch is similar to C_D of a cylinder for smaller Re. We found that at a constant Reynolds number, the least porous patch has the most energy released per vortex shedding period.

Increasing the spacing ratio leads to a reduction in the drag force and drag coefficient. For a high spacing ratio, the interactions of root wake are weak, and the flow pattern behind the patches is similar to a single cylinder. For a lower spacing ratio and dense patch, the drag force changed quadratically with upstream velocity and the characteristic length is equal to patch diameter, but for high spacing ratios, the force varies linearly with velocity and the patch has features of small Reynolds numbers with the characteristic length of root diameter. The velocity profile, for the lower values of spacing ratios, changes somewhat with respect to Reynolds number. Nevertheless, for the higher spacing ratios, the velocity profile behind the patch has the same pattern for different Re and is less dependent on the Re. For $\frac{L}{d} < 4.5$ we noticed a patch effect in a U-shaped velocity pattern behind the patches. Furthermore, by decreasing the spacing ratio, the wake length scale gets shorter. In contrast, for high spacing ratios, the U-shape velocity pattern disappears and the velocity profile resembles the behavior of flow around a single rigid cylinder, which is in agreement with the force results.

Within the flexibility experiment, the flexibility of the mangrove root has a quadratic relationship with the drag force and coefficient. Greater flexibility results in more drag force and higher drag coefficient to the patch. It can be inferred from the fact that by having more flexibility, the stem roots enlarge the frontal area, which has a direct impact on increasing the exerted force on the patch. As drag coefficient depends on the flexibility of the roots, it suggests that the flow resistance in mangrove vegetation in shallow water will depend on the flexibility. Yet, in the region of deep water with higher velocity, the flow resistance changes slightly with the flexibility of the mangrove prop roots.

The velocity behind less flexible roots starts from a minimum velocity and accelerates to reach the free stream velocity and the patch effect will disappear. However, for highly flexible patches, the velocity deficit is higher, and it requires greater distances to recover to free stream velocity in the downstream. Thus, the length scale of the velocity deficit region behind the patch of highly flexible roots is larger compared to

the corresponding rigid cases. Understanding the hydrodynamics of mangrove-like structures can elucidate the primary mechanisms for its resilience and by which mangrove roots are able to withstand high-energy fluid conditions. This information has the potential to improve future coastal infrastructure with bio-mimetic mangrove-like structures.

Acknowledgment

The authors wish to thank Samantha Parry for her help with constructing the soap film setup and data collection. Support for this project was generously provided by Link Foundation Ocean Engineering and Instrumentation PhD Fellowship. This work was also partially supported by an FAU seed grant to OMC and KVDR.

ORCID iDs

Amirkhosro Kazemi https://orcid.org/0000-0001-6967-3893

References

[1] Gedan K B, Kirwan M L, Wolanski E, Barbier E B and Silliman B R 2011 The present and future role of coastal wetland vegetation in protecting shorelines: answering recent challenges to the paradigm *Clim. Change* **106** 7–29
[2] Smith T J, Anderson G H, Balentine K, Tiling G, Ward G A and Whelan K R T 2009 Cumulative impacts of hurricanes on Florida mangrove ecosystems: sediment deposition, storm surges and vegetation *Wetlands* **29** 24–34
[3] Mazda Y, Magi M, Kogo M and Hong P N 1997 Mangroves as coastal protection from waves in the Tong King delta, Vietnam *Mangroves Salt Marshes* **1** 127–35
[4] Quartel S, Kroon A, Augustinus P G E F, Van Santen P and Tri N H 2007 Wave attenuation in coastal mangroves in the Red River Delta, Vietnam *J. Asian Earth Sci.* **29** 576–84
[5] Wolanski E 1995 Sediment transport in mangrove swamps *Hidrobiologii* **295** 51–8
[6] Mazda Y, Kanazawa N and Kurokawa T 1999 Dependence of dispersion on vegetation density in a tidal creek–mangrove swamp system *Mangroves Salt Marshes* **3** 59–66
[7] Mazda Y, Kanazawa N and Wolanski E 1995 Tidal asymmetry in mangrove creeks *Hydrobiologia* **295** 51–8
[8] Nagelkerken I, De Schryver A M, Verweij M C, Dahdouh-Guebas F, van der Velde G and Koedam N 2010 Differences in root architecture influence attraction of fishes to mangroves: a field experiment mimicking roots of different length, orientation, and complexity *J. Exp. Mar. Biol. Ecol.* **396** 27–34
[9] Kazemi A and Curet O 2016 PIV measurements and flow characteristics downstream of mangrove root models *APS Division of Fluid Dynamics (Fall) 2016, Abstract #D3.005 (Portland)* (https://doi.org/10.1103/BAPS.2016.DFD.D3.5)
[10] Mazda Y, Kobashi D and Okada S 2005 Tidal-scale hydrodynamics within mangrove swamps *Wetl. Ecol. Manag.* **13** 647–55
[11] Mazda Y and Wolanski E 2009 Hydrodynamics and modeling of water flow in mangrove areas *Coastal Wetlands: An Integrated Ecosystem Approach* (Amsterdam: Elsevier) pp 231–61
[12] Wolmski E, Jones M and Bunt J S 1980 Hydrodynamics of a tidal creek–mangrove swamp system *Mar. Freshw. Res.* **31** 431–50
[13] Zhang X, Chua V P and Cheong H F 2015 Hydrodynamics in mangrove prop roots and their physical properties *J. Hydro Environ. Res.* **9** 281–94
[14] Struve J, Falconer R A and Wu Y 2003 Influence of model mangrove trees on the hydrodynamics in a flume *Estuarine Coast. Shelf Sci.* **58** 163–71
[15] Wu Y, Falconer R A and Struve J 2001 Mathematical modelling of tidal currents in mangrove forests *Environ. Model. Softw.* **16** 19–29
[16] Mazda Y, Wolanski E, King B, Sase A, Ohtsuka D and Magi M 1997 Drag force due to vegetation in mangrove swamps *Mangroves Salt Marshes* **1** 193–9
[17] Kathiresan K and Bingham B L 2001 Biology of mangroves and mangrove ecosystems *Adv. Mar. Biol.* **40** 81–251
[18] Siniscalchi F and Nikora V I 2012 Flow-plant interactions in open-channel flows: a comparative analysis of five freshwater plant species *Water Resour. Res.* **48** 1–13
[19] Takemura T and Tanaka N 2007 Flow structures and drag characteristics of a colony-type emergent roughness model mounted on a flat plate in uniform flow *Fluid Dyn. Res.* **39** 694–710
[20] Zong L and Nepf H 2011 Vortex development behind a finite porous obstruction in a channel *J. Fluid Mech.* **691** 368–91
[21] Chen Z, Ortiz A, Zong L and Nepf H 2012 The wake structure behind a porous obstruction and its implications for deposition near a finite patch of emergent vegetation *Water Resour. Res.* **48** W09517
[22] Vandenbruwaene W, Maris T, Cox T J S, Cahoon D R, Meire P and Temmerman S 2011 Sedimentation and response to sea-level rise of a restored marsh with reduced tidal exchange: comparison with a natural tidal marsh *Geomorphology* **130** 115–26
[23] Nepf H M and Koch E W 1999 Vertical secondary flows in submersed plant-like arrays *Limnol. Oceanogr.* **44** 1072–80
[24] Sharpe R G and James C S 2006 Deposition of sediment from suspension in emergent vegetation *Water SA* **32** 211–8
[25] Tanino Y H N 2008 Laboratory investigation on mean drag in a random array of rigid, emergent cylinders *J. Hydraul. Eng.* **134** 4–41
[26] Sheridan J, Lin J-C and Rockwell D 1997 Flow past a cylinder close to a free surface *J. Fluid Mech.* **330** 1–30
[27] Zong L and Nepf H 2010 Flow and deposition in and around a finite patch of vegetation *Geomorphology* **116** 363–72
[28] Ortiz A C, Ashton A and Nepf H 2013 Mean and turbulent velocity fields near rigid and flexible plants and the implications for deposition *J. Geophys. Res.: Earth Surface* **118** 2585–99
[29] Follett E M and Nepf H M 2012 Geomorphology sediment patterns near a model patch of reedy emergent vegetation *Geomorphology* **179** 141–51
[30] Kazemi A, Parry S, van de Riet K and Curet O 2015 The effect of porosity and flexibility on the hydrodynamics behind a mangrove-like root model *68th Annual Meeting of the APS Division of Fluid Dynamics (Fall) 2015, Abstract #A25.007* (Boston, MA: APS Division of Fluid Dynamics) vol 60 p 21
[31] Nicolle A and Eames I 2011 Numerical study of flow through and around a circular array of cylinders *J. Fluid Mech.* **679** 1–31
[32] Kobashi D and Mazda Y 2005 Tidal flow in riverine-type mangroves *Wetl. Ecol. Manage.* **13** 615–9
[33] Furukawa K, Wolanski E and Mueller H 1997 Currents and sediment transport in mangrove forests *Estuarine Coast. Shelf Sci.* **44** 301–10
[34] Strusińska-Correia A, Husrin S and Oumeraci H 2013 Tsunami damping by mangrove forest: a laboratory study using parameterized trees *J. Nat. Hazards Earth Syst. Sci.* **13** 483–503
[35] White B L and Nepf H M 2007 Shear instability and coherent structures in shallow flow adjacent to a porous layer *J. Fluid Mech.* **593** 1–32
[36] Gharib M and Beizaie M 1999 Visualization of two dimensional flows by a liquid (soap) film tunnel *J. Vis.* **2** 119–26
[37] Beizaie M and Gharib M 1997 Fundamentals of a liquid (soap) film tunnel *Exp. Fluids* **23** 130–40
[38] Muijres F T and Lentink D 2010 Wake visualization of a heaving and pitching foil in a soap film *Animal Locomotion* ed G K Taylor, M S Triantafyllo, C Tropea pp 27–35
[39] Munson B R and Young D R 2006 *Fundamental of Fluid Mechanics* (New York: Wiley)
[40] Batham J P, Nakamura Y, Tomonari Y, Fey U, König M, Eckelmann H, Ahlborn B, Seto M L and Noack B R 2002 On drag, Strouhal number and vortex street structure *J. Fluid Mech.* **30** 363–78